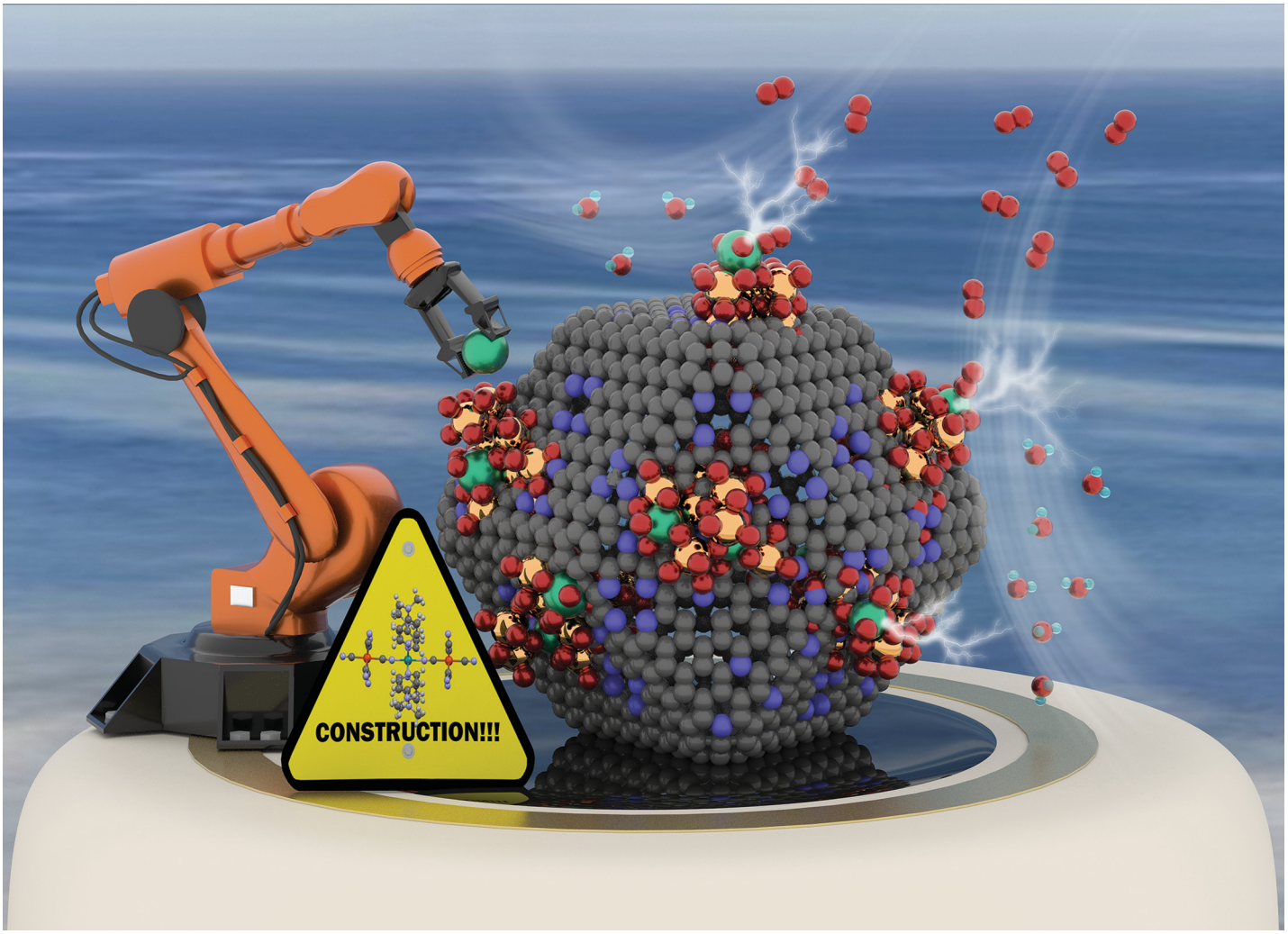

Showcasing research from Professor Shaowei Chen's laboratory, Department of Chemistry and Biochemistry, University of California, Santa Cruz, USA.

Oxygen reduction reaction catalyzed by carbon composites with ruthenium-doped iron oxide nanoparticles

Carbon nanocomposites based on transition-metal oxides have been recognized as cost-effective catalysts towards the oxygen reduction reaction (ORR). Herein, RuFe-NC nanocomposites are synthesized by controlled pyrolysis of a Fe–Ru–Fe trinuclear complex along with zeolitic imidazolate framework-8, which feature Ru-doped Fe_2O_3 nanoparticles embedded within a carbon scaffold, and exhibit an ORR activity in alkaline media rivaling that of commercial Pt/C. The use of the trinuclear complex facilitates the atomic dispersion of ruthenium within the Fe_2O_3 nanoparticles, and charge transfer between the metal centers leads to a high ORR activity.

As featured in:

See Shaowei Chen *et al.*, *Mater. Adv.*, 2022, **3**, 4556.

ROYAL SOCIETY OF CHEMISTRY

rsc.li/materials-advances

Registered charity number: 207890

Materials Advances

ROYAL SOCIETY OF CHEMISTRY

PAPER

View Article Online
View Journal | View Issue

Cite this: *Mater. Adv.*, 2022, 3, 4556

Oxygen reduction reaction catalyzed by carbon composites with ruthenium-doped iron oxide nanoparticles†

Qiming Liu,[a] Hong Bo Zhou,[ab] Forrest Nichols,[a] Han-Lin Kuo,[c] Rene Mercado,[a] Bingzhang Lu,[a] Weiya Zhu,[a] Yashu Liu,[ad] Jennifer Q. Lu,[c] Frank Bridges[e] and Shaowei Chen *[a]

Carbon nanocomposites based on transition-metal oxides have been attracting extensive attention as cost-effective catalysts towards the oxygen reduction reaction (ORR). However, the activity remains subpar as compared to state-of-the-art platinum catalysts. One way to enhance the ORR performance is to dope a second metal into the nanocomposite to manipulate the electronic structure and hence the interactions with key reaction intermediates. Herein, dual metal (Ru and Fe) and nitrogen codoped carbon (RuFe-NC) nanocomposites were synthesized by controlled pyrolysis of a Fe–Ru–Fe trinuclear complex along with zeolitic imidazolate framework-8. The obtained porous nanocomposites consisted of Ru-doped Fe_2O_3 nanoparticles embedded within a carbon scaffold, and exhibited an ORR activity in alkaline media rivaling that of commercial Pt/C, which was also markedly better than those of the monometallic counterparts and nanocomposites prepared with a simple mixture of the individual monometallic compound precursors. Structural characterization suggests that the use of the trinuclear complex facilitated the atomic dispersion of ruthenium within the iron oxide nanoparticles and charge transfer between the metal centers led to a high ORR activity. Results from this study suggest that rational design of heteronuclear complexes may be a unique strategy in the structural engineering of carbon-metal nanocomposites for high-performance electrocatalysis.

Received 18th January 2022,
Accepted 11th April 2022

DOI: 10.1039/d2ma00054g

rsc.li/materials-advances

Introduction

Fuel cell technologies have been attracting extensive interest as an integral part of the sustainable economy.[1] In fuel cell operation, small molecule fuels are oxidized at the anode and oxygen is reduced at the cathode, where both reactions necessitate appropriate catalysts so as to boost the electron-transfer kinetics and produce a sufficiently high current density for practical applications.[2–5] Of these, the oxygen reduction reaction (ORR) at the cathode has been recognized as a major bottleneck that limits the fuel cell performance, largely because of the complex reaction pathways and sluggish electron-transfer kinetics. Towards this end, platinum-based nanoparticles have been used extensively as the catalysts of choice for the ORR.[4–7] Yet, the high cost and low natural abundance of platinum have significantly hampered the wide-spread application of fuel cell technologies. Thus, in recent studies, a range of strategies have been developed to reduce the metal loadings (and costs) and concurrently retain/enhance the catalytic activity.[8–13] One effective route is to exploit low-cost 3d transition metals (*i.e.*, Fe, Co, Ni, and Cu) and their derivatives (*i.e.*, oxides, carbides, and nitrides) as the catalytic active centers.[14–17]

Among these various candidates, transition metal oxides (TMOs) have been extensively investigated with promising advances.[18–21] Nevertheless, it should be noted that the intrinsic activity of TMOs has remained mostly uncompetitive to that of the commercial Pt/C benchmark. For instance, theoretical studies based on first principles calculations have shown that the FeO_5, CoO_5, and NiO_5 centers are too weak for the adsorption of O* species, while CrO_5 and MnO_5 are too strong rendering the desorption of O* difficult, owing to their different electronic structures.[22] Thus, none of these is ideal for ORR electrocatalysis. To increase their activity towards ORR, a variety of strategies have been utilized to modify TMOs. For example, Wu *et al.*[23] grew Fe_3O_4 nanoparticles on N-doped

[a] *Department of Chemistry and Biochemistry, University of California, 1156 High Street, Santa Cruz, California 95064, USA. E-mail: shaowei@ucsc.edu*
[b] *School of Chemistry and Chemical Engineering, Jiangsu University, Zhenjiang, Jiangsu 212013, China*
[c] *School of Engineering, University of California, 5200 North Lake Road, Merced, California 95343, USA*
[d] *School of Environmental and Chemical Engineering, Jiangsu University of Science and Technology, Zhenjiang, Jiangsu 212013, China*
[e] *Department of Physics, University of California, 1156 High Street, Santa Cruz, California 95064, USA*

† Electronic supplementary information (ESI) available: Additional experimental data. See DOI: https://doi.org/10.1039/d2ma00054g

graphene aerogel and found that the substrate significantly increased the onset potential and cathodic current density, in contrast to those with (undoped) carbon black. Ma *et al.*[24] also observed that with N-doped carbon black, ultrafine $FeO_{1.4}$ nanoparticles exhibited an ORR activity competitive to that of Pt/C. Fan *et al.*[25] showed that the carbon substrate could benefit FeO_x with rapid mass transfer and catalyst stability.

In addition to structural engineering of the substrate, compositional manipulation of the oxide materials is another viable route with dual- or even tri-metal centers, where the metal-to-metal charge transfer can be exploited for enhanced electrical conductivity and improved ORR activity. For instance, Gao *et al.*[26] atomically dispersed Pt on α-Fe_2O_3 and observed a dramatically enhanced ORR activity with a half-wave potential ($E_{1/2}$) of +1.05 V *vs.* reversible hydrogen electrode (RHE), owning to the strong electronic coupling of the Pt–Fe atomic pairs. Such a synergistic effect facilitated the adsorption of O_2 and dissociation of the O═O bonds. Wei *et al.*[27] found that Ru dopants could facilitate O_2 adsorption on Co_3O_4 and significantly improve the ORR activity with $E_{1/2}$ increased from +0.32 to +0.77 V. In fact, Ru has been widely utilized as dopants of TMOs in various oxygen-involved reactions, due to its optimal affinity to oxygen intermediate species.[8,28] Theoretical calculations have shown that Ru can serve as the active sites on SnO_2 for the adsorption of oxygen species owning to the delocalization of electrons.[29] Dong *et al.*[30] also showed that Ru could regulate the charge transfer among the Cr, Co, and oxygen species. That is, the introduction of Ru into TMOs may tune their electronic structures and improve the ORR activity due to enhanced interactions with O*.

Herein, nanocomposites based on Ru-doped Fe_2O_3 nanoparticles supported on porous N-doped carbon were prepared by controlled pyrolysis of a Fe–Ru–Fe trinuclear complex ($[[(DMAP)_4Ru^{II}\{(\mu\text{-}NC)Fe^{III}(CN)_5\}_2](PPh_4)_4$, $Ru(LFe)_2$, with DMAP = 4-(dimethylamino)pyridine and PPh_4 = tetraphenylphosphonium)[31] as the metal sources and zeolitic imidazolate framework-8 (ZIF-8) as the carbon and nitrogen precursor. The resulting RuFe-NC nanocomposites exhibited a hierarchical porous structure, with abundant nitrogen dopants in the carbon scaffold and Ru homogeneously doped into the Fe_2O_3 nanoparticles. By contrast, for the control sample prepared with a physical mixture of ZIF-8 and individual Fe and Ru metal salts at equivalent feeds, partial phase segregation was observed between Fe and Ru. Notably, in alkaline media, RuFe-NC displayed an ORR activity rivalling that of commercial Pt/C and was the best among the metal,nitrogen-codoped carbon composites. Results from this study highlight the significance of pre-designed metal precursors in spatial control of dual metal oxide nanoparticles in carbon nanocomposites for high-performance electrocatalysis.

Experimental section

Chemicals

Dichlorotetrakis(dimethylsulfoxide)ruthenium(II) (*cis*-$Ru(DMSO)_4Cl_2$), tetraphenylphosphonium ferricyanide ($(PPh_4)_3[Fe(CN)_6]$), $Ru(LFe)_2$, and ZIF-8 were prepared according to methods described in the literature.[31,32] All other chemicals and reagents were commercially available and used as received without further purification. Water was supplied with a Barnstead Nanopure Water system (18 MΩ cm).

Sample preparation

To prepare the RuFe-NC composites, 0.1 g (0.4 mmol) of ZIF-8 was mixed with 0.01 g (0.004 mmol) of $Ru(LFe)_2$ synthesized above in 10 mL of hexane under sonication for 10 min and then under magnetic stirring for 2 h at room temperature. The solid was then collected by centrifugation at 6000 rpm for 5 min and dried under vacuum at 50 °C for 12 h. The resulting ZIF-8@$Ru(LFe)_2$ precursor was then loaded onto a ceramic boat, which was transferred to a tube furnace and heated at 900 °C for 2 h under a nitrogen atmosphere, producing RuFe-NC.

A series of control samples were prepared in the same fashion: (i) NC by direct pyrolysis of ZIF-8, (ii) Ru-NC by a mixture of 0.1 g (0.4 mmol) of ZIF-8, 0.002 g (0.004 mmol) of *cis*-$Ru(DMSO)_4Cl_2$, and 0.003 g of DMAP, (iii) Fe-NC by 0.1 g (0.4 mmol) of ZIF-8 and 0.01 g $(PPh_4)_3[Fe(CN)_6]$, and (iv) RuFe-NC_{mix} by 0.1 g (0.4 mmol) of ZIF-8, 0.002 g (0.004 mmol) of *cis*-$Ru(DMSO)_4Cl_2$, 0.003 g of DMAP and 0.01 g of $(PPh_4)_3[Fe(CN)_6]$.

Characterizations

Transmission electron microscopic (TEM) measurements were carried out on a JEOL JEM-2100F electron microscope. Scanning electron microscopy (SEM) and energy dispersive spectroscopic (EDS) mapping studies were carried out with an Apreo SEM microscope. X-ray diffraction (XRD) patterns were acquired with a Bruker D8 Advance diffractometer with Cu K_α radiation (λ = 0.15418 nm). X-ray photoelectron spectra (XPS) were obtained with a PHI-5400 XPS instrument with an Al K_α source operated at 350 W and 10^{-9} Torr. X-ray absorption spectroscopy (XAS) measurements were carried out at 10 K on beamline 4–1 at the Stanford Synchrotron Radiation Light source using an Oxford liquid helium cryostat. Nitrogen sorption isotherms were acquired with a Micromeritics ASAP 2020 porosimetry system at 77.3 K. UV-Vis absorption spectra were collected on a PerkinElmer Lambda 35 UV-vis spectrometer. Infrared spectroscopic measurements were conducted with a PerkinElmer Spectrum One FTIR spectrometer. Inductively coupled plasma-optical emission spectrometry (ICP-OES) measurements were conducted with an iCap 7400 analyzer.

Electrochemistry

The electrochemical tests were carried out on a CHI 710 electrochemical workstation in a standard three-electrode configuration. A graphite rod was used as the counter electrode, a Ag/AgCl in 0.1 M KCl as the reference electrode, and a polished rotating (gold) ring-(glassy carbon) disk electrode (RRDE, from Pine Instrument Co.) as the working electrode. The Ag/AgCl electrode was calibrated against an RHE and all potentials in the present study were referenced to this RHE. During the ORR tests, the ring potential was set at +1.5 V *vs.* RHE. To prepare the catalyst inks, 2 mg of the samples obtained above was added into 1 mL of an isopropanol/water (3 : 1 v/v) mixture and 10 μL of a 100 wt% Nafion solution.

The suspension was sonicated to form a homogeneous ink. 20 μL of the ink was then dropcast onto the glassy carbon disk electrode (surface area 0.246 cm^2), dried at room temperature, and coated with 5 μL of a 20 wt% Nafion solution, corresponding to a catalyst loading of 0.162 mg cm^{-2}. A same loading of commercial 20% Pt/C was used in the test.

Results and discussion

Synthesis and morphological characterization

The synthetic procedure of the RuFe-NC composite consists of three major steps, as shown in Scheme 1. The first step is the synthesis of the $Ru(LFe)_2$ trinuclear complex by simple refluxing of *cis*-$Ru(DMSO)_4Cl_2$, DMAP, and $(PPh_4)_3[Fe(CN)_6]$ (Fig. S1–S3, ESI†),[31] where one Ru atom is bridged by two cyanide (CN) ligands to two Fe centers. Second, rhombic dodecahedral ZIF-8 crystals were synthesized by mixing 2-methylimidazole and zinc nitrate salts,[33,34] onto which was adsorbed the $Ru(LFe)_2$ complex in hexane. Third, controlled pyrolysis of the ZIF-8@$Ru(LFe)_2$ mixture at 900 °C for 2 h in a nitrogen atmosphere led to the production of porous carbons doped with Ru and Fe (RuFe-NC). Control samples of RuFe-NC_{mix}, Ru-NC, Fe-NC, and NC were synthesized in the same fashion.

The porous structure of RuFe-NC was confirmed by Brunauer–Emmett–Teller (BET) measurements. As shown in Fig. 1a, the RuFe-NC, RuFe-NC_{mix}, Ru-NC, Fe-NC, and NC samples all exhibited an H_4-type hysteresis loop in the N_2 sorption isotherms, suggesting the formation of a mesoporous structure within the carbon matrices, and RuFe-NC shows an abrupt increase of the adsorbed N_2 quantity at relatively low pressures, indicative of a large number of micropores. Notably, the specific surface area varied markedly among the sample series, 507.6 $m^2\ g^{-1}$ for RuFe-NC, 540.2 $m^2\ g^{-1}$ for RuFe-NC_{mix}, 452.3 $m^2\ g^{-1}$ for Ru-NC, 442.7 $m^2\ g^{-1}$ for Fe-NC, and only 163.2 $m^2\ g^{-1}$ for NC, suggesting that the metal precursors actually behaved as effective porogens due to the high thermal volatility.[35] In addition, by the nonlocal density functional theory (NLDFT), the pore size distributions were then derived and depicted in Fig. 1b. Both RuFe-NC and NC can be seen to entail mesopores in the range of 1 to 2 nm, while RuFe-NC_{mix} has a large portion of micropores at 0.8 nm. As for both Ru-NC and Fe-NC, the micropore fraction was relatively small, in comparison to the dual-metal counterparts. The RuFe-NC sample also showed a larger fraction of mesopores and lower fraction of micropores than NC, as confirmed from the cumulative pore volume in Fig. S4 (ESI†). The enhanced surface area and porosity of the metal-containing nanocomposites is anticipated to facilitate mass transfer and accessibility of the catalytic active sites,[35] as demonstrated below in electrochemical measurements.

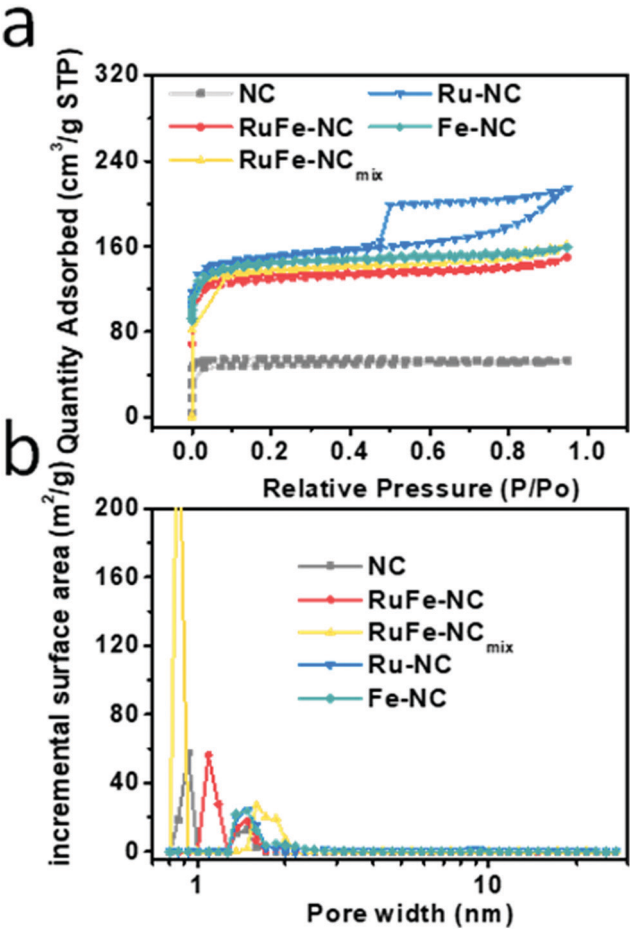

Fig. 1 (a) Nitrogen sorption isotherms of RuFe-NC, RuFe-NC_{mix}, Ru-NC, Fe-NC, and NC, and (b) the corresponding pore size distribution profiles.

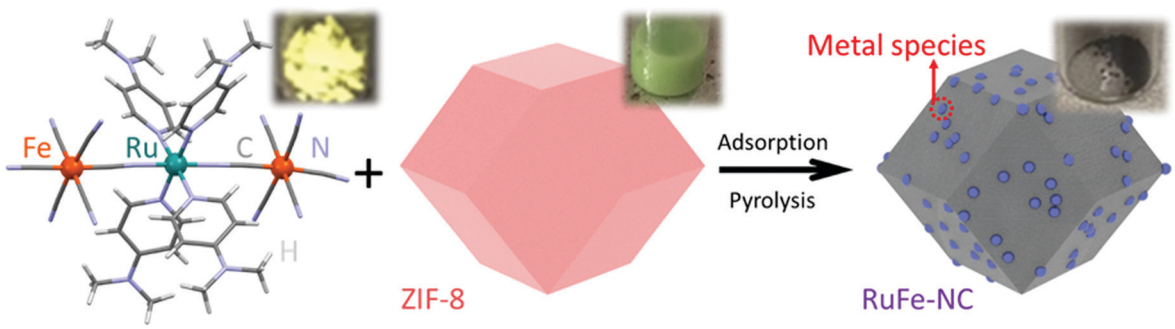

Scheme 1 Molecular structure of the $Ru(LFe)_2$ complex and the synthetic procedure of the RuFe-NC composite. Insets show the photographs of the products at different reaction stages.

Further structural insights were obtained from TEM measurements. One can see from Fig. 2a and b that the RuFe-NC sample partially retained the dodecahedral shape of the ZIF-8 precursor, exhibiting a lateral length of several hundred nm with an apparent porous structure (as highlighted by the pink circles in Fig. 2a). At higher magnifications (Fig. 2c and Fig. S5, ESI†), one can find nanoparticles of *ca.* 2 nm in diameter that were encapsulated with a graphitized carbon shell. These nanoparticles exhibited well-defined lattice fringes, with a *d* spacing of *ca.* 0.220 and 0.235 nm that may be ascribed to the (113) and (400) facets of Fe_2O_3 (PDF#32-0469, red dashed circles),[36] respectively. It should be noted that no apparent RuO_2 or Ru nanoparticles can be found, and both *d* spacings are slightly larger than those of standard hematite Fe_2O_3, likely due to the doping of Ru into the iron oxide lattices (Fig. S5–S7, ESI†). Meanwhile, graphitized carbon can be seen to show a hemispherical shape with a *d* spacing of 0.338 nm (blue circle), corresponding to the (002) facet of graphitized carbon (JCPDS No. 01-0646).[37,38] Furthermore, in elemental mapping analysis (Fig. 2d and Fig. S8, ESI†), it can be seen that Ru was mostly confined within the dark-contrast nanoparticles, consistent with the notion that Ru was doped into Fe_2O_3 nanoparticles. In addition, the RuFe-NC sample was found to consist of *ca.* 0.9 at% of Fe and 0.3 at% of Ru (Fig. S9, ESI†).

A similar structural morphology was observed with the Ru-NC (Fig. S10, ESI†), Fe-NC (Fig. S11, ESI†), and RuFe-NC_{mix} samples (Fig. S12, ESI†). Notably, the RuFe-NC_{mix} composite can be seen to consist of nanoparticles of *ca.* 4 nm in diameter embedded within the carbon sheets (Fig. S13, ESI†). Elemental mapping analysis of the selected area (Fig. S13, ESI†) showed a homogeneous distribution of C and N, while the elements of Fe and O were concentrated in the bright regions in the dark-field image, suggesting the formation of FeO_x nanoparticles. Yet, the distribution pattern of ruthenium was different from that of Fe, suggesting partial segregation between these two elements. Furthermore, EDS measurements (Fig. S14, ESI†) showed that the RuFe-NC_{mix} sample consisted of *ca.* 0.6 at% of Fe and 0.3 at% of Ru, consistent with the initial feed ratio. A similar sheet-like structure was observed withe both Ru-NC (Fig. S8, ESI†) and Fe-NC (Fig. S9, ESI†), which also featured metal oxide particles with a diameter of around 5 nm on the carbon sheets. Note that the nanoparticles were all markedly larger in these control samples than those in RuFe-NC, likely because of the bonding constraint in the $Ru(LFe)_2$ complex precursor (Scheme 1) and the geometric confinement by the micropores (Fig. 1b) in the pyrolytic preparation of RuFe-NC.

X-ray spectroscopy analysis

XRD measurements were then carried out to examine the graphitization of the samples prepared by high-temperature pyrolysis. From Fig. 3, all samples can be seen to exhibit two broad diffraction peaks at $2\theta \approx 23^\circ$ and 43°, which can be assigned to the (002) and (100) facets of graphite (JCPDS No. 01-0646), in good agreement with results from TEM measurements (Fig. 2c). No Additional diffraction peaks of metal or metal oxides can be discerned from the XRD profiles, most likely due to the low contents as detected in EDS measurements (Fig. S9 and S14, ESI†) and the small size of the nanoparticles (Fig. 2 and Fig. S5, ESI†).

XPS measurements were further performed to determine the elemental composition and valence states of the samples. From

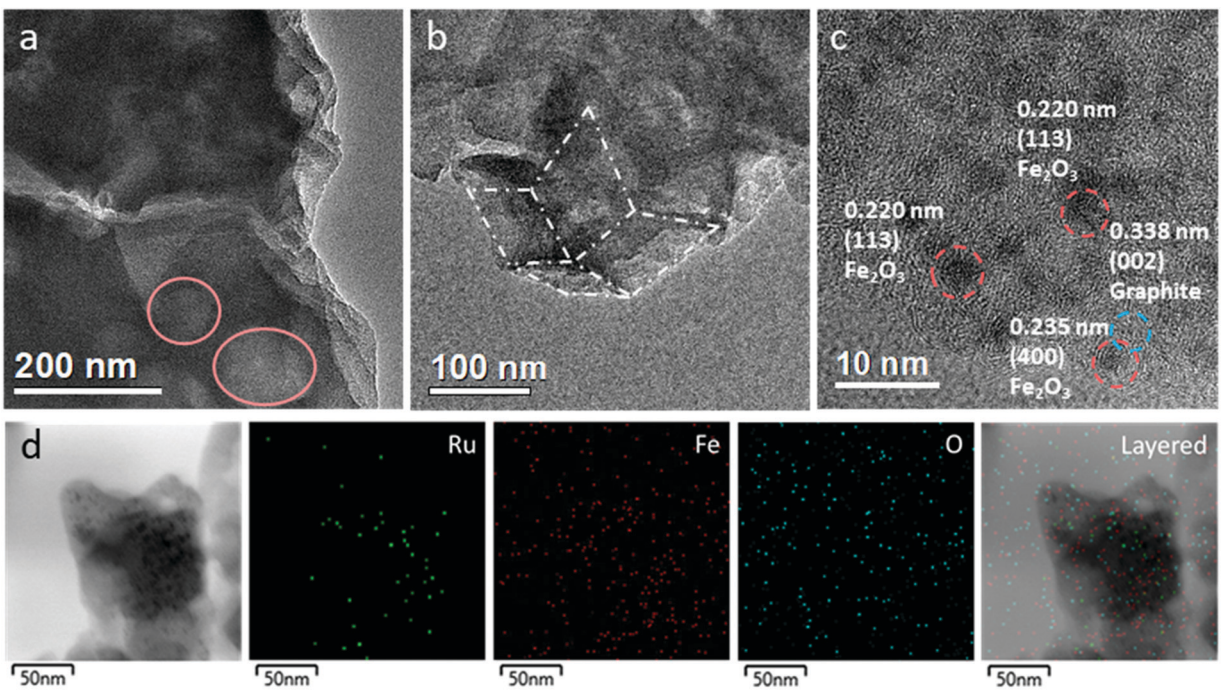

Fig. 2 (a–c) Representative TEM images of RuFe-NC at varied magnifications. The pink circles highlight the microporous structure of the carbon matrix. (d) Representative TEM image of RuFe-NC and the corresponding EDS elemental maps of Ru, Fe, and O.

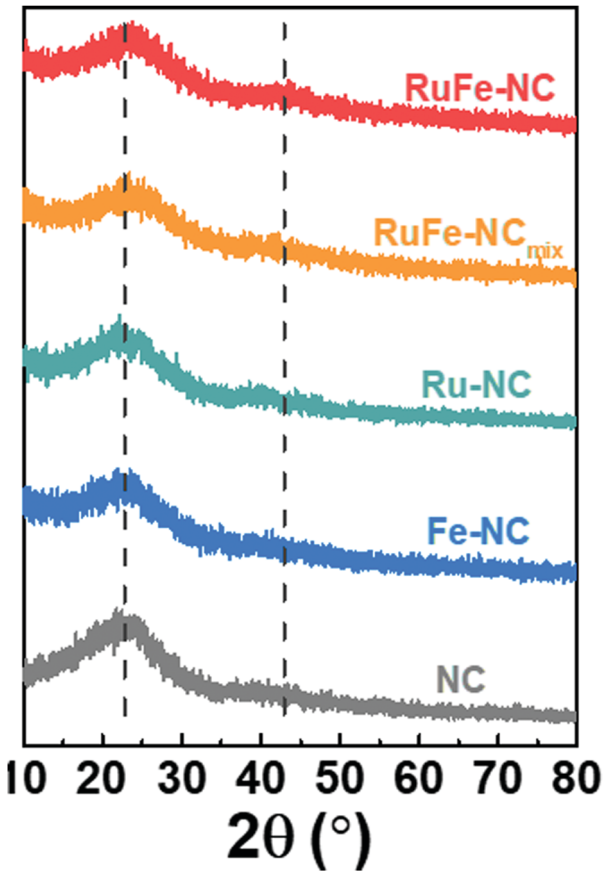

Fig. 3 XRD patterns of RuFe-NC, RuFe-NC$_{mix}$, Ru-NC, Fe-NC, and NC. The dashed lines indicate the expected 2θ position of the (002) and (100) diffractions of graphite (JCPDS No. 01-0646). Units on the y-axis have arbitrary units.

the survey spectra of RuFe-NC and RuFe-NC$_{mix}$ in Fig. S15 (ESI†), the C 1s, N 1s, and O 1s electrons can be readily identified at *ca.* 285 eV, 398 eV, and 531 eV, respectively. Fig. 4a depicts the high-resolution Fe 2p spectra of the Ru(LFe)$_2$ complex, RuFe-NC, RuFe-NC$_{mix}$, and Fe-NC, where the Fe 2p$_{3/2}$ peaks of RuFe-NC (711.51 eV), RuFe-NC$_{mix}$ (711.26 eV) and Fe-NC (711.31 eV) can be found to blue-shift by *ca.* 2 eV in comparison to that of the Ru(LFe)$_2$ complex (709.38 eV), suggesting an increase of the Fe valence state from Fe(II) in the complex to Fe(III) in the pyrolytic products.[39,40]

As for the Ru 3d spectra in Fig. 4b, RuFe-NC, RuFe-NC$_{mix}$ and Ru-NC showed a small shoulder near 280.30 eV, which is *ca.* 0.6 eV lower than that of the Ru(LFe)$_2$ complex (280.90 eV), suggesting partial reduction (electron enrichment) of ruthenium(II) in the complex precursor after pyrolysis (*i.e.*, the Ru valence state in RuFe-NC was between 0 and +2).[37,41] Notably, the Ru 3d binding energy of RuFe-NC and RuFe-NC$_{mix}$ was *ca.* 0.15 eV lower than that of Ru-NC (280.45 eV). This observation, in conjunction with the variation of the Fe(III) 2p$_{3/2}$ binding energy of RuFe-NC (711.51 eV) > RuFe-NC$_{mix}$ (711.26 eV) ≈ Fe-NC (711.31 eV), suggests charge transfer from Fe to Ru in the Fe_2O_3 nanoparticles of RuFe-NC, which diminished in RuFe-NC$_{mix}$ due to segregated distributions of Fe and Ru (Fig. 2 and Fig. S11, ESI†). In fact, metallic Fe was even found in RuFe-NC$_{mix}$ (706.89 eV, 0.068 at%, Fig. 4a).

In addition, based on the integrated peak areas, the elemental compositions of the samples were also evaluated. The Fe content was estimated to be *ca.* 1.97 wt% (0.45 at%) for RuFe-NC and 2.35 wt% (0.59 at%) for RuFe-NC$_{mix}$, close to the results from ICP-OES (1.69 wt% and 2.64 wt%, respectively) and EDS measurements (vide ante, Fig. S9 and S14, ESI†).

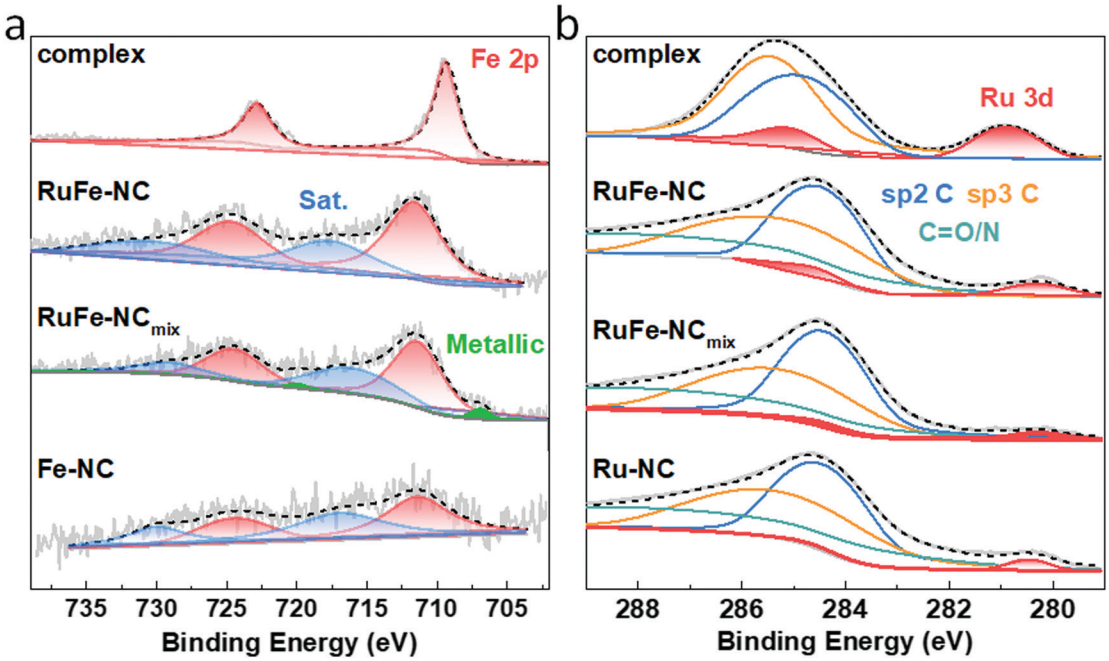

Fig. 4 (a) High-resolution XPS spectra of the Fe 2p electrons of the RuFe complex, RuFe-NC, RuFe-NC$_{mix}$, and Fe-NC. (b) High-resolution XPS spectra of the C 1s and Ru 3d electrons of RuFe complex, RuFe-NC, RuFe-NC$_{mix}$, and Ru-NC. Note, the y-axis is logarithmic.

The corresponding Ru content was *ca.* 0.50 wt% for RuFe-NC, somewhat higher than that from EDS analysis (Fig. S9, ESI†), and 0.34 wt% for RuFe-NC_{mix} that was consistent with the EDS results (Fig. S14, ESI†). This suggests Ru enrichment on the surface of RuFe-NC as compared to that of RuFe-NC_{mix}.

From the C 1s spectra in Fig. 4b, one can see that the samples all consists of a large amount (284.63 eV, 38.9 at%) of sp^2-hybridized C, along with sp^3 C (285.69 eV) and C═O/N (288.80 eV), suggesting successful graphitization of the ZIF-8 precursors.[34] The N 1s spectrum of RuFe-NC is shown in Fig. S16 (ESI†), which can be deconvoluted into four peaks at 398.3 eV for pyridinic N, 399.7 eV for pyrrolic N, 400.8 eV for graphitic N, and 403.4 eV for oxidized N, with an atomic content of 2.0, 1.7, 2.0, and 1.2 at%, respectively (6.9 at% in total). With such abundant pyridinic N and pyrrolic N moieties, it is possible that part of the Fe species was coordinated to those N moieties. In fact, from the O 1s spectra in Fig. S17 (ESI†), RuFe-NC can be seen to entail a small metal-O shoulder, which accounted for 0.20 at% of the sample, corresponding to 0.13 at% Fe in Fe_2O_3, which suggests that the rest of about 0.32 at% of Fe was in the form of FeN_x moieties. Such a metal-lattice O component was markedly more pronounced with RuFe-NC_{mix}, which was estimated to be 0.92 at%, *ca.* 1.75 times that of Fe in FeO_x (0.53 at%), very close to the atomic ratio of 1.5 in Fe_2O_3. This suggests that the Fe species in RuFe-NC_{mix} was mostly in the form of Fe_2O_3 (Fig. S13, ESI†), with a minor component of metallic Fe and no FeN_x moieties.[42] These results are also listed in Table S1–S6 (ESI†).

Further structural insights were obtained in XAS measurements. From the Fe K edge spectra in Fig. 5a, one can see that RuFe-NC exhibited a similar pre-edge profile and post-edge oscillations to Fe_2O_3, suggesting an analogous chemical environment of the Fe centers. In fact, both RuFe-NC and (hematite) Fe_2O_3 can be seen to display a small pre-edge peak at 7113 eV (magenta arrow) arising from the 1s to 3d forbidden electric dipole transition, consistent with an octahedral coordination shell in the samples,[43,44] in sharp contrast to Fe foil which featured an intense shoulder in the pre-edge region. The Ru K edge spectra are depicted in Fig. 5b. One can see that the main edge energy of RuFe-NC was lower than that of RuO_2, but higher than that of Ru foil, suggesting electron enrichment of Ru in RuFe-NC in comparison to RuO_2. These observations are consistent with results from the XPS measurements which suggested Fe to Ru charge transfer in the composites.

The corresponding R space EXAFS spectra are shown in Fig. 5c and d. One can see that the peak patterns, again, are very similar between RuFe-NC and Fe_2O_3. In the Fe R space spectrum of RuFe-NC (Fig. 5c), two main peaks can be identified at *ca.* 1.42 and 2.70 Å, which can be assigned to the Fe–O/N bonds and second-shell Fe–Fe/Ru, respectively, in good agreement with the formation of (Ru-doped) Fe_2O_3 nanoparticles and FeN_x moieties, as suggested in XPS measurements (Fig. 4). From the fitting results (Fig. S18a and Table S7, ESI†), one can see that that the Fe–O/N bonds in RuFe-NC possessed a coordination number of 4.8 with a bond length of 2.00 Å, while the Fe–Fe/Ru linkage featured a coordination number of 2.0 with a bond length of 2.95 Å. These fitting results are consistent with the small size and poor crystallinity of the Ru-doped Fe_2O_3 nanoparticles, and the formation of FeN_x moieties as speculated in TEM and XPS measurements (vide ante). In the corresponding Ru EXAFS data (Fig. 5d), Ru of RuFe-NC displayed an apparently different pattern from those of Ru foil and RuO_2. Three major species can be resolved in RuFe-NC, *i.e.*, Ru–O (shoulder, *ca.* 1.3 Å), Ru–P (1.81 Å), and Ru–Ru (2.61 Å). These lengths are approximately 0.3 Å shorter than the realized bond length due to the well-known phase shift in EXAFS. Ru-doped α-Fe_2O_3 was used to calculate the FEFF functions of the Ru–O and Ru–Fe standard paths for EXAFS fitting. Data of the RuFe-NC sample was fitted by using two distinct structures, Ru-doped α-Fe_2O_3 and tetragonal RuP_3, where the former accounted for *ca.* 80% in the sample and 20% for the latter.[45] As shown in Fig. S18b and Table S7 (ESI†), one can see that the Ru–O bond possessed a coordination number of 2.5 with a bond length of 2.04 Å, which is larger than the typical Ru–O bond length of RuO_2 (1.98 Å)[46,47] and closer to that of M–O bond of hematite. The Ru–Fe path featured a coordination number of 1.16 and a bond length of 2.99 Å, which is smaller than the Ru–Ru bond length in RuO_2 (3.3 Å) but closer to the one in hematite (2.97 Å), suggesting the successful incorporation of Ru into α-Fe_2O_3. Note that the low coordination number of Ru–O (2.51) is strong evidence for significant disorder in α-Fe_2O_3, likely due to the small oxide particle size and presence of amorphous iron oxide within the sample. Also, the fact that the peak at *ca.* 3.2 Å observed with RuO_2 was absent in RuFe-NC suggests atomic dispersion of Ru into the Fe_2O_3 nanoparticles, as proposed in the above TEM and XPS measurements.

Electrocatalytic activity

The ORR activity of the obtained samples was then examined by electrochemical measurements. All samples displayed a similar cyclic voltammetric (CV) profile in N_2-saturated 0.1 M KOH that is free of redox features, most likely due to the low content of the metal species (Fig. S19, ESI†). From the linear sweep voltammograms (LSV) acquired in rotating ring-disk electrode (RRDE) measurements in O_2-saturated 0.1 M KOH (Fig. 6a), all composite samples with metal dopants can be seen to exhibit an apparently better ORR performance than the metal-free NC, and the dual-metal samples, RuFe-NC and RuFe-NC_{mix}, display a further enhanced performance in comparison with the monometal counterparts of Ru-NC and Fe-NC. Remarkably, RuFe-NC stood out as the best ORR catalyst among the series. For instance, Ru-NC exhibited an onset potential (E_{onset}) of +0.90 V, *ca.* 60 mV more positive than that of NC, but the half-wave potential was slightly inferior ($E_{1/2}$ = +0.62 V *vs.* +0.64 V). Fe-NC was significantly more active towards ORR, with an E_{onset} of +0.94 V and $E_{1/2}$ of +0.81 V, which were similar to those of RuFe-NC_{mix} (though the latter actually showed a much higher diffusion current density of *ca.* 4 mA cm^{-2} than other monometal-doped samples). This suggests that iron oxides played a dominant role in these samples in ORR electrocatalysis.[23,25] Notably, an even better ORR activity was observed with RuFe-NC, where the performance (E_{onset} = +0.99 V, $E_{1/2}$ = +0.87 V) was actually

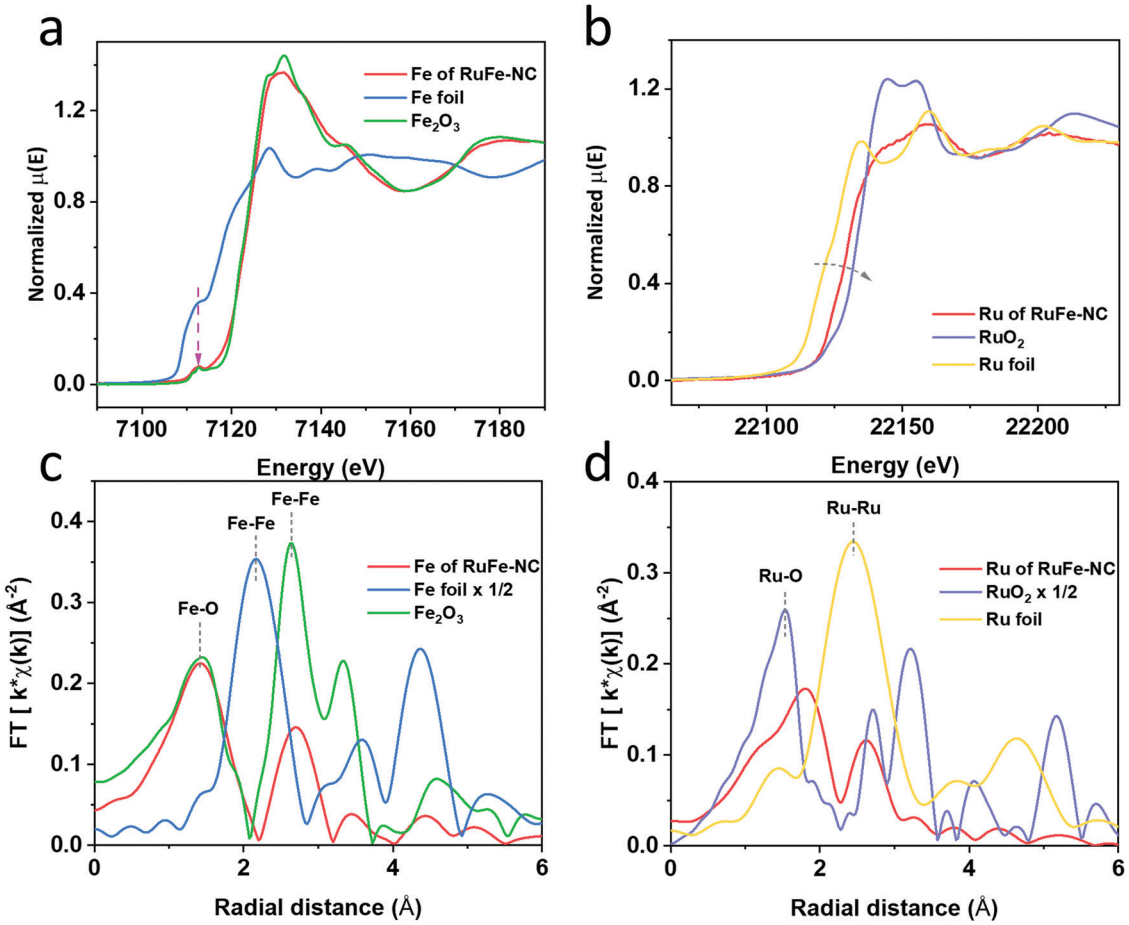

Fig. 5 X-ray absorption near-edge spectra (XANES): (a) Fe K edge of RuFe-NC, Fe foil, and Fe_2O_3 (hematite); (b) Ru K edge of RuFe-NC, Ru foil, and RuO_2. Corresponding extended X-ray absorption fine structure (EXAFS) spectra of (c) Fe of RuFe-NC, Fe foil, and Fe_2O_3; (d) Ru of RuFe-NC, Ru foil, and RuO_2.

highly comparable to commercial Pt/C (E_{onset} = +1.00 V, $E_{1/2}$ = +0.87 V), suggesting the significance of Ru doping in Fe_2O_3 nanoparticles in enhancing the ORR activity of RuFe-NC likely due to the Fe–Ru charge transfer. It should be noted that increasing or decreasing the $Ru(LFe)_2$ loading in the sample preparation actually led to a diminished ORR performance, suggesting that RuFe-NC represented the optimal composite (Fig. S20, ESI†).

To gain further insights into the ORR electrocatalysis, the number of electron transfer (n) and H_2O_2% yield were evaluated by $n = \frac{4i_D}{i_D + i_R/N}$ and $H_2O_2\% = \frac{200i_R/N}{i_D + i_R/N}$, respectively, where i_R and i_D are the ring current and disk current, and N is the collection efficiency of the ring electrode (0.40). One can see from Fig. 6b that at +0.8 V the n value is *ca.* 3.98 with an ultralow H_2O_2% of 0.65% for RuFe-NC, suggestive of the four-electron pathway of ORR. The performance of RuFe-NC_{mix} was a close second, with n = 3.98 and a slightly higher H_2O_2% of 0.95%. Note that these are even better than that of commercial Pt/C (n = 3.92, H_2O_2% = 3.82%). In contrast, a substantially lower performance was observed with Fe-NC (n = 3.97 and H_2O_2% = 1.40%) and Ru-NC (n = 3.88, H_2O_2% = 5.81%). In the Tafel plots (Fig. 6c), RuFe-NC can be seen to display a Tafel slope of 80.7 mV dec^{-1}, which is close to that of Pt/C (79.0 mV dec^{-1}), indicating highly efficient electron-transfer kinetics where the first electron reduction of oxygen was likely the rate-determining step.[34,40,48] Notably, the Tafel slope was greater for RuFe-NC_{mix} at 102 mV dec^{-1}, and markedly higher for Ru-NC (189 mV dec^{-1}) and Fe-NC (122 mV dec^{-1}), indicating a diminishing ability to cleave the O–O bonds during the ORR process.[49]

The effective electrochemical surface areas of the samples were then evaluated by the electrode double-layer capacitance (C_{dl}). Within the potential range of +0.9 to +1.1 V (*i.e.*, a non-faradaic region), CVs were acquired at scan rates varied from 10 to 60 mV s^{-1} (Fig. S21, ESI†), from which the corresponding C_{dl} was derived. One can see from Fig. 6d that RuFe-NC possessed the largest C_{dl} of 25.1 mF cm^{-2}, over two times those of other samples (*ca.* 11.6 mF cm^{-2}). This is consistent with the porous structure as manifested in the above BET and TEM measurements, which is beneficial to increase the accessibility to the catalytically active sites.

The robustness of the active sites of RuFe-NC was then tested by repeated potential cycling between +0.6 and +1.0 V.

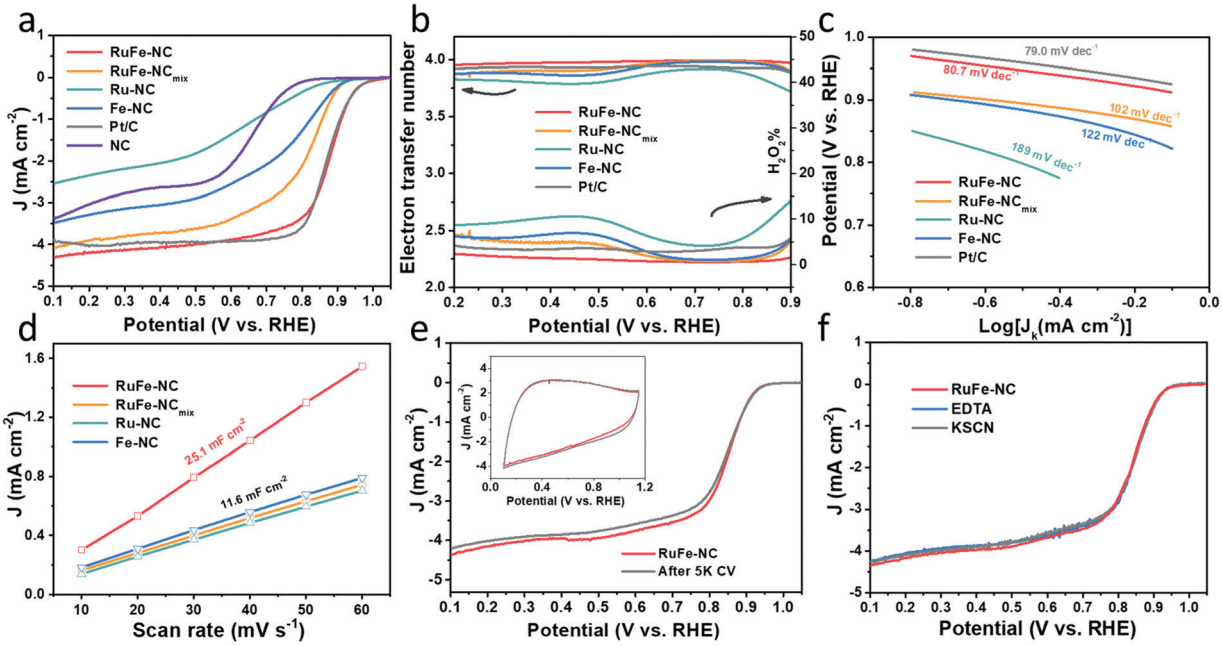

Fig. 6 ORR performance of the RuFe-NC and control samples in oxygen-saturated 0.1 M KOH. (a) Linear sweep voltammograms (LSVs) of RuFe-NC and control samples of RuFe-NC$_{mix}$, Ru-NC, Fe-NC, Pt/C, and NC at the rotation rate of 1600 rpm. (b) The corresponding electron-transfer number (n, left *y*-axis), the yield of H_2O_2 (%, right *y*-axis), and (c) Tafel plots with the slopes shown in mV dec^{-1}. (d) Double layer capacitances (C_{dl}) of selected samples. (e) Stability test of RuFe-NC for 5000 cycles in N_2-saturated 0.1 M KOH. Inset is the corresponding cyclic voltammograms at the scan rate of 50 mV s^{-1} before and after the stability test. (f) Poisoning test of RuFe-NC with EDTA and KSCN treatments.

After 5000 cycles, there were only minimal changes of the voltammograms (inset to Fig. 6e) and a slight shift of the diffusion-limited current density (less than 5%) in the corresponding LSV curve, manifesting excellent catalyst durability. After 10 000 cycles, the activity of RuFe-NC decayed somewhat with a cathodic shift of $E_{1/2}$ by 50 mV (Fig. S22, ESI†), but remained better than those of a number of relevant catalysts reported recently in the literature (Table S8, ESI†). Furthermore, the RuFe-NC catalysts exhibited remarkable tolerance against poisoning species like KSCN or EDTA, where negligible changes were discerned upon the addition of such poisoning species into the electrolyte (Fig. 6f). A similar behavior was observed with RuFe-NC$_{mix}$ (Fig. S23, ESI†). Such an anti-poisoning property against SCN^- might be due to the unique structure of the Ru-doped Fe_2O_3 nanoparticles where the O-rich surface rendered the binding of SCN^- ligands difficult. Meanwhile, as a hexadentate ligand, EDTA mostly chelates mononuclear metal centers, and the minimal impacts on the ORR performance suggests that Fe single atoms (*e.g.*, FeN_x) are unlikely the dominant active sites.[37,50] These results further confirm that the Ru-doped Fe_2O_3 nanoparticles, rather than the FeN_x moieties, were responsible for the ORR activity, within the present experimental context.

Mechanistically, the remarkable ORR activity most likely arose from the Fe to Ru charge transfer in Ru-doped Fe_2O_3, owing to their different electronegativity. In fact, electron depletion of Fe within Fe_2O_3 has been demonstrated as an effective strategy to manipulate the spin states of the Fe centers, generate partially occupied e_g orbital and facilitate the adsorption of O_2.[26,51–53] In the present study, the atomic dispersion of Ru within RuFe-NC facilitated such charge transfer and hence enhanced the ORR activity, in contrast to the RuFe-NC$_{mix}$ sample where apparent segregation of Ru and Fe occurred.

In fact, when RuFe-NC was subject to acid leaching with 0.5 M H_2SO_4 at 80 °C for 4 h, the ORR activity was markedly diminished, with E_{onset} = +0.93 V and $E_{1/2}$ = +0.74 V (Fig. 7), a negative shift of 130 mV as compared to the as-prepared sample. These results demonstrate, again, the dominant

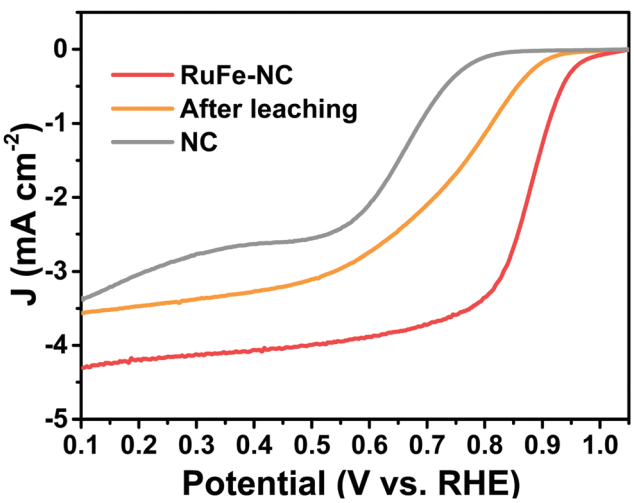

Fig. 7 LSV curves of RuFe-NC in 0.1 M KOH before and after acid leaching treatment, in comparison to that of NC.

contributions of metal oxide nanoparticles in the RuFe-NC composite to the ORR activity, with a minor contribution from the FeN_x moieties (as manifested by the leached sample which contained mainly atomically disperse FeN_x moieties but still outperformed the metal-free NC).

Conclusions

In this study, a trinuclear $Ru(LFe)_2$ complex was used as the metal precursor to prepare carbon nanocomposites with Ru-doped Fe_2O_3 nanoparticles, as confirmed in a range of microscopic and spectroscopic measurements. The obtained RuFe-NC nanocomposites exhibited an excellent ORR activity, with an E_{onset} of +0.99 V and an $E_{1/2}$ of +0.87 V, which is comparable to that of the state-of-the-art Pt/C catalyst. Notably, the ORR activity was also markedly better than those of the monometal counterparts and samples prepared with a simple physical mixture of the relevant metal salts (where partial segregation of the metal species occurred). This was accounted for by the Fe to Ru charge transfer in the RuFe-NC composites that was advantageous for the adsorption of key reaction intermediates and enhanced electrochemical surface area that facilitated the accessibility of the catalytic active sites. Results from this study suggest that rational design of the metal precursors may be exploited as an effective strategy in manipulating the morphological and electronic structure of carbon for high-performance electrocatalysis.

Author contributions

Qiming Liu: writing – original draft, sample preparation, data acquisition and analysis. Hongbo Zhou: preparation of $Ru(LFe)_2$ complex. Forrest Nichols and Frank Bridges: acquisition and analysis of X-ray absorption data. Han-Lin Kuo and Jennifer Q. Lu: acquisition of TEM images and elemental mapping analysis. Rene Mercado, Bingzhang Lu, Weiya Zhu, and Yashu Liu: assistance in data acquisition and results discussion. Shaowei Chen: conception of project, results analysis, writing – review & editing.

Conflicts of interest

There are no conflicts to declare.

Acknowledgements

This work was supported, in part, by the National Science Foundation (CHE-1900235 and CHE-2003685). TEM, XPS and BET studies were carried out as part of a user project at the National Center for Electron Microscopy and Molecular Foundry of Lawrence Berkeley National Laboratory which is supported by the Office of Science, Office of Basic Energy Sciences, of the US Department of Energy under Contract No. DE-AC02-05CH11231. The XAS experiments were performed at the Stanford Synchrotron Radiation Lightsource (SSRL), which is supported by the US Department of Energy, Office of Science, Office of Basic Energy Sciences under Contract No. DE-AC02-76SF00515. The authors also thank Jeremy Barnett for the assistance in sample preparation and data acquisition in XRD measurements using the X-ray Facility at the University of California Santa Cruz funded by the National Science Foundation (MRI-1126845).

References

1 K. I. Ozoemena and S. W. Chen, Nanomaterials for Fuel Cell Catalysis. in *Nanostructure Science and Technology*, Springer International Publishing: Cham, 1st edn, 2016.
2 M. Shao, Q. Chang, J. P. Dodelet and R. Chenitz, *Chem. Rev.*, 2016, **116**, 3594–3657.
3 Z. Y. Lu, B. F. Wang, Y. F. Hu, W. Liu, Y. F. Zhao, R. O. Yang, Z. P. Li, J. Luo, B. Chi, Z. Jiang, M. S. Li, S. C. Mu, S. J. Liao, J. J. Zhang and X. L. Sun, *Angew. Chem., Int. Ed.*, 2019, **58**, 2622–2626.
4 A. Morozan, B. Jousselme and S. Palacin, *Energy Environ. Sci.*, 2011, **4**, 1238–1254.
5 X. J. Zhou, J. L. Qiao, L. Yang and J. J. Zhang, *Adv. Energy Mater.*, 2014, **4**, 1301523.
6 C. Du, X. H. Gao and W. Chen, *Chin. J. Catal.*, 2016, **37**, 1049–1061.
7 J. A. Trindell, Z. Y. Duan, G. Henkelman and R. M. Crooks, *Chem. Rev.*, 2020, **120**, 814–850.
8 H. S. Wang, Y. Yang, F. J. DiSalvo and H. D. Abruña, *ACS Catal.*, 2020, **10**, 4608–4616.
9 V. Stamenkovic, T. J. Schmidt, P. N. Ross and N. M. Markovic, *J. Phys. Chem. B*, 2002, **106**, 11970–11979.
10 Y. C. Xing, Y. Cai, M. B. Vukmirovic, W. P. Zhou, H. Karan, J. X. Wang and R. R. Adzic, *J. Phys. Chem. Lett.*, 2010, **1**, 3238–3242.
11 A. U. Nilekar, Y. Xu, J. L. Zhang, M. B. Vukmirovic, K. Sasaki, R. R. Adzic and M. Mavrikakis, *Top. Catal.*, 2007, **46**, 276–284.
12 Y. Xiong, Y. Yang, H. Joress, E. Padgett, U. Gupta, V. Yarlagadda, D. N. Agyeman-Budu, X. Huang, T. E. Moylan, R. Zeng, A. Kongkanand, F. A. Escobedo, J. D. Brock, F. J. DiSalvo, D. A. Muller and H. D. Abruna, *Proc. Natl. Acad. Sci. U. S. A.*, 2019, **116**, 1974–1983.
13 D. L. Wang, H. L. L. Xin, R. Hovden, H. S. Wang, Y. C. Yu, D. A. Muller, F. J. DiSalvo and H. D. Abruna, *Nat. Mater.*, 2013, **12**, 81–87.
14 E. L. Hu, X. Y. Yu, F. Chen, Y. D. Wu, Y. Hu and X. W. Lou, *Adv. Energy Mater.*, 2018, **8**, 1702476.
15 X. Han, Z. P. Zheng, J. Y. Chen, Y. K. Xue, H. Q. Li, J. Zheng, Z. X. Xie, Q. Kuang and L. S. Zheng, *Nanoscale*, 2019, **11**, 12610–12618.
16 W. J. Jiang, L. Gu, L. Li, Y. Zhang, X. Zhang, L. J. Zhang, J. Q. Wang, J. S. Hu, Z. D. Wei and L. J. Wan, *J. Am. Chem. Soc.*, 2016, **138**, 3570–3578.
17 H. S. Park, S. B. Han, D. H. Kwak, J. H. Han and K. W. Park, *J. Catal.*, 2019, **370**, 130–137.

18 A. Bonnefont, A. S. Ryabova, T. Schott, G. Kerangueven, S. Y. Istomin, E. V. Antipov and E. R. Savinova, *Curr. Opin. Electrochem.*, 2019, **14**, 23–31.
19 Y. J. Wang, H. B. Fan, A. Ignaszak, L. Zhang, S. Q. Shao, D. P. Wilkinson and J. J. Zhang, *Chem. Eng. J.*, 2018, **348**, 416–437.
20 Y. Wang, J. Li and Z. D. Wei, *J. Mater. Chem. A*, 2018, **6**, 8194–8209.
21 R. J. Toh, Z. Sofer and M. Pumera, *Chem. Phys. Chem.*, 2015, **16**, 3527–3531.
22 J. Hwang, R. R. Rao, L. Giordano, Y. Katayama, Y. Yu and Y. Shao-Horn, *Science*, 2017, **358**, 751–756.
23 Z. S. Wu, S. B. Yang, Y. Sun, K. Parvez, X. L. Feng and K. Mullen, *J. Am. Chem. Soc.*, 2012, **134**, 9082–9085.
24 Y. J. Ma, H. Wang, J. Key, V. Linkov, S. Ji, X. F. Mao, Q. Z. Wang and R. F. Wang, *Int. J. Hydrogen Energy*, 2014, **39**, 14777–14782.
25 Z. Y. Fan, J. Li, W. Yang, Q. Fu, K. Sun, Y. C. Song, Z. D. Wei, Q. Liao and X. Zhu, *Chem. Eng. J.*, 2020, **385**, 123393.
26 R. J. Gao, J. Wang, Z. F. Huang, R. R. Zhang, W. Wang, L. Pan, J. F. Zhang, W. K. Zhu, X. W. Zhang, C. X. Shi, J. Lim and J. J. Zou, *Nat. Energy*, 2021, **6**, 614–623.
27 M. R. Wei, S. Huang, Y. Wang, Y. H. Liu, Y. F. He, C. Wang and L. Yang, *J. Alloys Compd.*, 2020, **827**, 154207.
28 J. Yu, Q. J. He, G. M. Yang, W. Zhou, Z. P. Shao and M. Ni, *ACS Catal.*, 2019, **9**, 9973–10011.
29 Z. G. Zhu, R. C. Deka, A. Chutia, R. Sahnoun, H. Tsuboi, M. Koyama, N. Hatakeyama, A. Endou, H. Takaba, C. A. Del Carpio, M. Kubo and A. Miyamoto, *J. Phys. Chem. Solids*, 2009, **70**, 1248–1255.
30 C. L. Dong, X. L. Zhang, J. Xu, R. Si, J. Sheng, J. Luo, S. N. Zhang, W. J. Dong, G. B. Li, W. C. Wang and F. Q. Huang, *Small*, 2020, **16**, 1905328.
31 M. B. Rossi, K. A. Abboud, P. Albores and L. M. Baraldo, *Eur. J. Inorg. Chem.*, 2010, 5613–5616.
32 J. Wang, Z. Q. Huang, W. Liu, C. R. Chang, H. L. Tang, Z. J. Li, W. X. Chen, C. J. Jia, T. Yao, S. Q. Wei, Y. Wu and Y. D. Lie, *J. Am. Chem. Soc.*, 2017, **139**, 17281–17284.
33 J. Yang, Z. Y. Qiu, C. M. Zhao, W. C. Wei, W. X. Chen, Z. J. Li, Y. T. Qu, J. C. Dong, J. Luo, Z. Y. Li and Y. Wu, *Angew. Chem., Int. Ed.*, 2018, **57**, 14095–14100.
34 Q. M. Liu, Y. Peng, Q. X. Li, T. He, D. Morris, F. Nichols, R. Mercado, P. Zhang and S. W. Chen, *ACS Appl. Mater. Interfaces*, 2020, **12**, 17641–17650.
35 S. H. Lee, J. Kim, D. Y. Chung, J. M. Yoo, H. S. Lee, M. J. Kim, B. S. Mun, S. G. Kwon, Y. E. Sung and T. Hyeon, *J. Am. Chem. Soc.*, 2019, **141**, 2035–2045.
36 B. D. Adams and A. C. Chen, *Mater. Today*, 2011, **14**, 282–289.
37 B. Z. Lu, L. Guo, F. Wu, Y. Peng, J. E. Lu, T. J. Smart, N. Wang, Y. Z. Finfrock, D. Morris, P. Zhang, N. Li, P. Gao, Y. Ping and S. W. Chen, *Nat. Commun.*, 2019, **10**, 631.
38 F. Liu, S. Y. Song, D. F. Xue and H. J. Zhang, *Adv. Mater.*, 2012, **24**, 1089–1094.
39 X. Tian, X. Zhao, Y. Su, L. Wang, H. Wang, D. Dang, B. Chi, H. Liu, E. J. Hensen and X. W. D. Lou, *Science*, 2019, **366**, 850–856.
40 B. Z. Lu, T. J. Smart, D. D. Qin, J. E. Lu, N. Wang, L. M. Chen, Y. Peng, Y. Ping and S. W. Chen, *Chem. Mater.*, 2017, **29**, 5617–5628.
41 D. J. Morgan, *Surf. Interface Anal.*, 2015, **47**, 1072–1079.
42 D. Flak, Q. L. Chen, B. S. Mun, Z. Liu, M. Rekas and A. Braun, *Appl. Surf. Sci.*, 2018, **455**, 1019–1028.
43 T. E. Westre, P. Kennepohl, J. G. DeWitt, B. Hedman, K. O. Hodgson and E. I. Solomon, *J. Am. Chem. Soc.*, 1997, **119**, 6297–6314.
44 L. X. Chen, T. Liu, M. C. Thurnauer, R. Csencsits and T. Rajh, *J. Phys. Chem. B*, 2002, **106**, 8539–8546.
45 B. K. Teo, *EXAFS: basic principles and data analysis*, Springer Science & Business Media, 2012.
46 C. H. Zhang, J. W. Sha, H. L. Fei, M. J. Liu, S. Yazdi, J. B. Zhang, Q. F. Zhong, X. L. Zou, N. Q. Zhao, H. S. Yu, Z. Jiang, E. Ringe, B. I. Yakobson, J. C. Dong, D. L. Chen and J. M. Tour, *ACS Nano*, 2017, **11**, 6930–6941.
47 M. A. Hubert, A. M. Patel, A. Gallo, Y. Z. Liu, E. Valle, M. Ben-Naim, J. Sanchez, D. Sokaras, R. Sinclair, J. K. Norskov, L. A. King, M. Bajdich and T. F. Jaramillo, *ACS Catal.*, 2020, **10**, 12182–12196.
48 B. Lu, Q. Liu, F. Nichols, R. Mercado, D. Morris, N. Li, P. Zhang, P. Gao, Y. Ping and S. W. Chen, *Research*, 2020, **2020**, 9167829.
49 J. Chlistunoff, *J. Phys. Chem. C*, 2011, **115**, 6496–6507.
50 J. Wang, X. M. Ge, Z. L. Liu, L. Thia, Y. Yan, W. Xiao and X. Wang, *J. Am. Chem. Soc.*, 2017, **139**, 1878–1884.
51 S. Y. Chen, Y. Yan, P. P. Hao, M. H. Li, J. Y. Liang, J. Guo, Y. Zhang, S. W. Chen, W. P. Ding and X. F. Guo, *ACS Appl. Mater. Interfaces*, 2020, **12**, 12686–12695.
52 R. J. Gao, L. Pan, Z. W. Li, C. X. Shi, Y. D. Yao, X. W. Zhang and J. J. Zou, *Adv. Funct. Mater.*, 2020, **30**, 1910539.
53 G. Q. Shen, R. R. Zhang, L. Pan, F. Hou, Y. J. Zhao, Z. Y. Shen, W. B. Mi, C. X. Shi, Q. F. Wang, X. W. Zhang and J. J. Zou, *Angew. Chem., Int. Ed.*, 2020, **59**, 2313–2317.